# **Uncertainty Estimates for SeaSonde HF Radar Ocean Current Observations**

#### **BRIAN EMERY**

Marine Science Institute, University of California, Santa Barbara, Santa Barbara, California

#### LIBE WASHBURN

Department of Geography, and Marine Science Institute, University of California, Santa Barbara, Santa Barbara, California

(Manuscript received 20 June 2018, in final form 20 November 2018)

#### ABSTRACT

HF radars typically produce maps of surface current velocities without estimates of the measurement uncertainties. Many users of HF radar data, including spill response and search and rescue operations, incorporate these observations into models and would thus benefit from quantified uncertainties. Using both simulations and coincident observations from the baseline between two operational SeaSonde HF radars, we demonstrate the utility of expressions for estimating the uncertainty in the direction obtained with the Multiple Signal Classification (MUSIC) algorithm. Simulations of radar backscatter using surface currents from the Regional Ocean Modeling System show a close correspondence between direction of arrival (DOA) errors and estimated uncertainties, with mean values of 15° at 10 dB, falling to less than 3° at 30 dB. Observations from two operational SeaSondes have average DOA uncertainties of 2.7° and 3.8°, with a fraction of the observations (10.5% and 7.1%, respectively) having uncertainties of >10°. Using DOA uncertainties for data quality control improves time series comparison statistics between the two radars, with  $r^2 = 0.6$  increasing to  $r^2 = 0.75$  and RMS difference decreasing from 15 to 12 cm s<sup>-1</sup>. The analysis illustrates the major sources of error in oceanographic HF radars and suggests that the DOA uncertainties are suitable for assimilation into numerical models.

# 1. Introduction

Oceanographic HF radars produce high-resolution maps of ocean surface currents that reveal complex ocean surface dynamics. The contribution of these maps to our understanding of coastal oceanography has been limited only by the fact that the measurement errors are essentially unquantified. The observations result from complex signal processing techniques that obscure the errors and their numerous sources. While many studies have put bounds on the errors, typically through comparisons with independent measurements, "further efforts to understand error structure in HF radar derived data are clearly warranted" (Oke et al. 2002, p. 5-8), and the HF radar community should "develop . . . uncertainty estimates so that search areas can be modeled more effectively" (O'Donnell et al. 2005, p. 7-4). In this paper we aim to further the understanding of error sources in oceanographic HF radars and to quantify the uncertainties.

Corresponding author: Brian Emery, brian.emery@ucsb.edu

Oceanographic HF radars typically use one of two methods for bearing determination: beamforming (Graber et al. 1997; Chapman et al. 1997; Gurgel et al. 1999) or direction finding (DF) with Multiple Signal Classification (MUSIC; Schmidt 1986). This analysis focuses on radars using the SeaSonde three-element receive antenna (manufactured by CODAR Ocean Sensors Ltd.), with MUSIC for direction finding [ongoing work seeks to extend this analysis to other array types, such as Wellen Radars (WERA; Gurgel et al. 1999) and the Least Expensive Radar (LERA; P. Flament et al. 2017, meeting presentation), but these results will be reported elsewhere]. While MUSIC has numerous advantages over beamforming, MUSIC encounters limitations with low SNR, small numbers of temporal samples, and small numbers of receive antenna elements-all common characteristics of the SeaSonde and its signal processing techniques. Further limitations result from closely spaced signal sources (Krim and Viberg 1996)—a potential characteristic of the ocean surface currents. It is not thoroughly understood how these limitations translate to observational uncertainties in the SeaSonde data.

Many investigations of oceanographic HF radar errors attempt to infer errors and uncertainties from comparisons with in situ current measurements. Following the methods of Graber et al. (1997), Chapman et al. (1997), and Chapman and Graber (1997), studies of radars employing MUSIC (e.g., Emery et al. 2004; Paduan et al. 2006; Liu et al. 2014) were able to attribute errors to the direction-finding technique. Other studies using in situ data demonstrated the importance of measured antenna patterns for decreasing error (Kohut and Glenn 2003; Cosoli et al. 2010), and that screening radial data by SNR improved comparisons with in situ measurements (Cosoli et al. 2012). In these examples geophysical differences between the measurements limited what could be attributed specifically to the radar processing, results further demonstrated by Kohut et al. (2006) with an ADCP, and Ohlmann et al. (2007) with drifters. To avoid these complicating factors, other studies adopted a simulation-based approach. Laws et al. (2000), and later de Paolo and Terrill (2007), looked at MUSIC performance using different ocean current scenarios with variable SNR. Cook et al. (2007) and Laws et al. (2010) investigated the influence of antenna pattern distortions on error. In these examples the SNR, the receive antenna pattern measurement (APM), and the receive antenna design were shown to affect the observational errors.

These studies did not address the longstanding needs for data-based metrics or uncertainty estimates. While the SeaSonde produces parameters along with observations (Lipa et al. 2006) that may be close to the final uncertainty product needed by modelers (D. E. Barrick 2013, personal communication), our preliminary work suggests that these are poor indicators of error. However, metrics based on properties of the MUSIC direction of arrival (DOA) function have been shown to improve comparison results when used for thresholding (Kirincich et al. 2012). These improvements are significant, particularly as quality control metrics, but they fall short of providing an uncertainty estimate with each velocity observation.

Outside of oceanography MUSIC has been thoroughly studied and several publications derive analytical expressions for DOA error. Stoica and Nehorai (1989) derived the DOA error variance based on a Taylor expansion of the MUSIC DOA function and the statistical properties of the eigenvectors of the data covariance matrix. Given this expression, it is possible to estimate the uncertainty for a given MUSIC DOA solution. In the context of oceanographic HF radars, the ability to produce a MUSIC solution along with an estimate of the directional error could go a long way toward meeting the needs of users as described above.

Several recent studies employ the techniques and results of Stoica and Nehorai (1989) to further the

understanding of oceanographic radars. Both Lai et al. (2017c) and Tian et al. (2017) derive an expression based on Taylor expansion of the MUSIC DOA function to quantify DOA errors resulting from the difference between the measured and ideal antenna patterns. They use the result to improve DOA estimation with the SeaSonde-like cross loop/monopole system known as the Ocean State Measuring and Analyzing Radar, type S (OSMAR-S). Furthermore, Lai et al. (2017a) attribute average bearing errors to differences between measured and ideal antenna patterns. These use ideal patterns in the MUSIC inversion. These studies further the understanding of the influence of antenna pattern distortions on DF data, but they do not attempt to assess the Stoica and Nehorai (1989) result for use as an operational error metric, or as an estimator of HF DOA error. Given that Stoica and Nehorai (1989) necessarily make simplifying assumptions about the signal environment that may or may not apply to oceanographic HF radars, it remains to be demonstrated that the theoretical error expressions predict the actual performance of oceanographic radars.

In this paper we evaluate methods for estimating uncertainties associated with the radial velocities produced by SeaSonde oceanographic HF radars. In section 2 we review the processing of oceanographic HF radar signals and present factors contributing to errors. In section 3 we present the simulation-based evaluation techniques. In section 4 we define the Stoica and Nehorai (1989) expressions for estimating DOA uncertainty. Results are presented in section 5, along with further discussion in section 6. Conclusions of the analysis are summarized in section 7, with mathematical symbols defined in appendix A and additional calculation details in appendix B.

## 2. Oceanographic HF radar processing and errors

Figure 1 summarizes the signal processing of oceanographic HF radar data up to radial velocity components  $\mathbf{v}_r$ . Boxes on the left are based on previous
publications [Fig. 1 from both Barrick and Lipa (1999)
and de Paolo and Terrill (2007)] and are specific to the
processing of SeaSonde data (Lipa et al. 2006). Other
operational HF radars use a slightly different scheme
with details specific to beamforming. However, it has
been shown that the scheme in Fig. 1 can be used for
somewhat arbitrary receive antenna configurations (e.g.,
P. Broche et al. 2004, meeting presentation; Barbin et al.
2006). Errors arise at several points as shown on the right
in Fig. 1. Here we describe the errors and uncertainties
that arise in HF radar observations, resulting from the
sequence of signal processing steps.

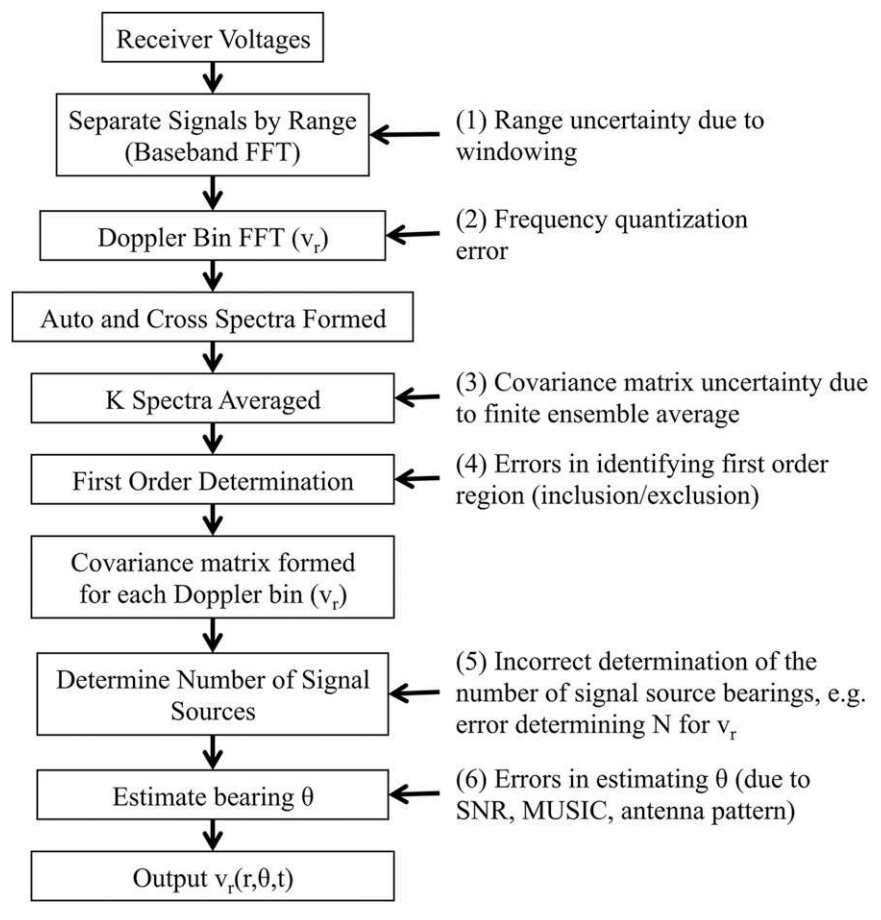


FIG. 1. HF radar data processing flow for estimating radial velocities, with error sources. [Adapted from Barrick and Lipa (1999) and de Paolo and Terrill (2007).]

1) Range uncertainty due to windowing. The first FFT of the antenna voltage time series separates signals by range (cf. Barrick and Lipa 1999). Assuming the conversion of a continuous flow field into discrete range rings can be understood as a discretization process, we can use the theory for analog-to-digital conversion to estimate error in the range determination. Given a range cell width Δr, the range uncertainty can be estimated (Bendat and Piersol 2000) as follows:

$$\sigma_{\mathbf{r}} = \sqrt{\frac{1}{12}} \Delta \mathbf{r} \approx 0.29 \Delta \mathbf{r}, \tag{1}$$

where the factor of 1/12 is the variance introduced when representing the uniformly distributed range with the discretized value. Furthermore, windowing (e.g., Hamming) applied to the frequency-modulated continuous-wave (FMCW) sweep to convert frequency to range causes 20% overlap in adjacent range cells (Lipa and Barrick 1983) and thus an

- increase in the range increment. In this case the range increment  $\Delta \mathbf{r}$  is increased by a factor of 1.2, and (1) becomes  $\sigma_{\mathbf{r}} = 0.35\Delta \mathbf{r}$ .
- 2) Frequency quantization error. For oceanographic radars signals arrive nearly simultaneously from all angles within view. FFT processing of the time series produced by step 1 sorts signal variance by Doppler frequencies, which are then processed by MUSIC separately. Given M antennas, the requirement for a noise subspace in the eigen decomposition limits MUSIC to processing N signal sources, where N < M. Thus, the FFT preprocessing allows a radar with just a few receive antennas (e.g., M = 3) to produce DOA solutions for many more than M signals in a given time period. After FFT processing, frequency components are then autoand cross multiplied to form power spectra (Lipa et al. 2006).

The FFT calculation and formation of cross-spectra (cf. Lipa et al. 2006; de Paolo et al. 2007) introduce errors in  $\mathbf{v}_r$  as a result of the discretization

of frequency bins. Using (1) but substituting  $\Delta \mathbf{v}_r$  for  $\Delta \mathbf{r}$ , we can estimate the velocity uncertainty using

$$\sigma_{\mathbf{v}} \approx 0.29 \Delta \mathbf{v}_{r}.$$
 (2)

Here  $\Delta \mathbf{v}_r$  is the radar radial velocity increment,

$$\Delta \mathbf{v}_r = \frac{\lambda_{\text{TX}}}{2} \frac{\text{SWR}}{n_{\text{FFT}}},\tag{3}$$

computed with the transmitted wavelength  $\lambda_{\rm TX}$ , the sweep rate (SWR), and the FFT length ( $n_{\rm FFT}$ ) (Lipa and Barrick 1983). For a radar with  $\Delta \mathbf{v}_r = 4.3 \, \mathrm{cm \, s}^{-1}$ ,  $\sigma_{\mathbf{v}_r} = 1.2 \, \mathrm{cm \, s}^{-1}$ , though longer FFTs reduce  $\sigma_{\mathbf{v}_r}$  to less than 1 cm s<sup>-1</sup> (Kirincich et al. 2012; Forget 2015).

- 3) Covariance matrix uncertainty due to finite ensemble averages. After cross multiplying, we average K cross-spectra (where K is the number of independent ensembles, or "snapshots"; Van Trees 2002) and form the covariance matrix **C**(f) for each frequency bin f (cf. de Paolo et al. 2007). Finite sampling periods and the dynamic nature of the ocean surface limit K. Uncertainty in the covariance matrix resulting from the choice of K influences the direction-finding estimate, contributing to DOA error, as discussed below.
- 4) Error in identifying first-order region. After forming the cross-spectra, we must determine what portion of the spectrum contains the signal from the first-order scattering process, which includes the ocean current information. To identify frequency bins containing the first-order signal, operational SeaSondes use empirical methods (Lipa and Barrick 1983), or image processing techniques (Kirincich 2017). Errors arise in two ways: 1) when the non-current, or signal is interpreted as originating from ocean currents or 2) when the signal from ocean currents is excluded from processing. These errors can be large in certain situations, such as when high winds ( $>15\,\mathrm{m\,s}^{-1}$ ) combine with strong currents (>2 m s<sup>-1</sup>), causing the first-order and second-order signal regions to become indistinguishable (CODAR 2002). On average, these errors are probably less than or equal to the reported 2–8 cm s<sup>-1</sup> noise levels based on estimates from the power spectra of the HF radar currents (Emery et al. 2004; Forget 2015).
- 5) Incorrect determination of the number of signal source bearings. Once the  $M \times M$  covariance matrix has been formed for Doppler bins in the first-order region, MUSIC uses the noise eigenvectors to determine the source DOA(s) (cf. Schmidt 1986; Tuncer and Friedlander 2009; Emery 2018, manuscript submitted to IEEE J. Oceanic Eng.). The SeaSonde uses a hypothesis testing approach to associate the eigenvectors with the signal or the noise,

determining whether the signal results from a single bearing N = 1 or from "dual" bearings N = 2 (Lipa and Barrick 1983). For both the SeaSonde and other arrays, the impact of incorrect determination of N has not been quantified. Another potential source of error is the possibility of the ocean surface presenting situations with  $N \ge M$ . The performance of MUSIC when  $N \ge M$  has not received much attention.

6) Error in estimating the DOA. Several factors contribute to errors in the DOA estimates from MUSIC, including the SNR, the accuracy and characteristics of the antenna pattern measurement, and the angular separation of the signal sources (cf. Van Trees 2002; Friedlander 2009). As mentioned above, limits on *K* used to form  $\mathbf{C}(f)$  produce uncertainty in both  $\mathbf{C}(f)$  and the DOA estimate. Average DOA errors in the range 0°–19° that have been shown for oceanographic HF radars (Kohut and Glenn 2003; Emery et al. 2004; Paduan et al. 2006; Cosoli et al. 2010; Kirincich et al. 2012; Lai et al. 2017a) likely result from these factors.

The above steps summarize the major sources of error in currents from oceanographic HF radars. Known methods for estimating the uncertainty contributed by steps 1 and 2 were included. In the following sections, we describe and evaluate analytical expressions for estimating the uncertainty resulting from steps 3 and 6. Errors resulting from steps 4 and 5 are not investigated here, and will require further analysis.

## 3. Signal models and simulation methods

## a. General array data model

To present expressions for the error variance, we must first define the data model and related notation. In the simplified case of N discrete signal sources (N < M), following Schmidt (1986) and Stoica and Nehorai (1989), we define the voltage time series measured at the receive antenna outputs  $\mathbf{Y}$  as the product of the N signal sources impinging on the array from bearings  $\theta_1, \theta_2, \ldots, \theta_N$  given by  $\mathbf{X}(t)$ , and the array response  $\mathbf{A}$ , plus noise  $\mathbf{e}(t)$ :

$$\mathbf{Y} = \mathbf{AX}(t) + \mathbf{e}(t). \tag{4}$$

Here the  $M \times N$  matrix **A** gives the response of the M antenna elements to each signal source,

$$\mathbf{A} = \begin{bmatrix} | & | & | \\ \mathbf{a}(\theta_1) & \mathbf{a}(\theta_2) & \dots & \mathbf{a}(\theta_N) \\ | & | & | \end{bmatrix}, \tag{5}$$

where the  $M \times 1$  vectors  $\mathbf{a}(\theta)$  represent the antenna pattern at each  $\theta$ . The matrix  $\mathbf{X}(t)$  gives the typically complex-valued signal from the N signal sources, described below.

Noise given by the matrix  $\mathbf{e}(t)$  is assumed to be Gaussian distributed with zero mean and variance  $\sigma^2$ . Given **A** at the source locations  $\theta_1, \ldots, \theta_N, \mathbf{X}(t)$ , and  $\mathbf{e}(t)$ , we compute **Y** with (4) and then the  $M \times M$  data covariance matrix,

$$\mathbf{C} = \frac{1}{K} \mathbf{Y} \mathbf{Y}^H, \tag{6}$$

where H denotes the Hermitian conjugate. The matrix  $\mathbf{C}$  forms the input to MUSIC. Expressions (4)–(6) define the data model for general  $\mathbf{X}(t)$ . This model holds for arbitrary receive antenna arrays, but in both simulations described below we use the ideal SeaSonde antenna pattern. The more complex simulations of ocean back-scatter require additional processing between (4) and (6) as we describe below. We first use (4) and (6) with a relatively simple  $\mathbf{X}(t)$ , which allows us to investigate error estimates in a simplified scenario.

#### b. Discrete source simulations

In the simplified discrete source simulations, we define  $\mathbf{X}(t)$  as an  $N \times K$  matrix,

$$\mathbf{X}(t) = \begin{bmatrix} x_1(t_1) & x_1(t_2) & \cdots & x_1(t_K) \\ \vdots & \ddots & & \vdots \\ x_N(t_1) & x_N(t_2) & \cdots & x_N(t_K) \end{bmatrix},$$
(7)

where each row represents a signal source time series. Each row [e.g.,  $x_N(t)$ ] is made up of K normally distributed random numbers with zero mean (Stoica and Moses 2005). This model defines independent discrete signal sources commonly used to test DOA methods (e.g., Van Trees 2002). The complex-valued matrix  $\mathbf{A}$  has dimensions  $M \times N$ , such that  $\mathbf{Y}$  is  $M \times K$ . For each Monte Carlo simulation, we vary both the values for sources  $[\mathbf{X}(t)]$ , and the complex-valued  $M \times K$  matrix  $\mathbf{e}(t)$  at a given SNR. When using this model, we ran 500 simulations at each value of SNR in the range 1–30 dB, with K = 9.

## c. Oceanographic radar simulations

For simulations of backscatter from oceanographic HF radars, we use a modified version of the signal model used in previous studies (Barrick and Lipa 1996; Laws et al. 2000; de Paolo et al. 2007; Laws et al. 2010). Following these we define  $\mathbf{X}(t)$ ,

$$\mathbf{X}(t) = \boldsymbol{\gamma}_{+} \exp[i(\boldsymbol{\omega}_{B} + \boldsymbol{\omega}_{c})t] + \boldsymbol{\gamma}_{-} \exp[i(-\boldsymbol{\omega}_{B} + \boldsymbol{\omega}_{c})t].$$
(8)

The expression (8) models the signal backscattered from the ocean surface, with the combined Doppler shift

resulting from the advancing and receding Bragg resonant waves  $\pm \omega_B$  and the currents  $\omega_c$ . We compute  $\omega_B = (2k_{\rm TX}g)^{1/2}$  based on the radar wavenumber  $k_{\rm TX} = 2\pi f_{\rm TX}/c$ , the radar transmit frequency  $f_{\rm TX}$ , the gravitational acceleration g, and the speed of light c. The radial component of the ocean surface current provides  ${\bf v}_r$  for computing  $\omega_c = 2k_{\rm TX}{\bf v}_r$ . The matrix  $\gamma_\pm$  defines a decorrelation factor, discussed below. Simulations used  $f_{\rm TX} = 13.45\,{\rm MHz}$  in the calculations, but the results do not depend on the transmit frequency.

A significant difference from the discrete source simulation is that  $\mathbf{X}(t)$  now has dimensions of  $N_{\mathbf{v}_r} \times n_{\text{FFT}}$ , where  $N_{\mathbf{v}_r}$  is the length of the vector  $\mathbf{v}_r$  and  $n_{\text{FFT}}$  specifies the length of the time series as typically produced by oceanographic HF radars. We interpolate  $\mathbf{A}$  to the  $N_{\mathbf{v}_r}$  positions in  $\theta$  for each value of  $\mathbf{v}_r(\theta)$ , such that (8) results in  $\mathbf{X}(t)$  with dimension  $N_{\mathbf{v}_r} \times n_{\text{FFT}}$  and  $\mathbf{Y}$  with dimension  $M \times n_{\text{FFT}}$ .

After forming  $\mathbf{Y}$ , we compute the FFTs of each row and then auto- and cross multiply these to form power and cross-spectra. After averaging K of these, we identify frequency bins containing the first-order signal with the methods of Kirincich (2017) and form the  $\mathbf{C}(f)$  for each frequency bin separately (cf. de Paolo et al. 2007) following the processing sequence outlined in Fig. 1.

In simulations for this study, we obtain  $\mathbf{v}_r$  from the surface velocity field of the Regional Ocean Modeling System (ROMS) (Shchepetkin and McWilliams 2005), as configured and run for Romero et al. (2016). As described by Romero et al. (2016), the one-way nesting scheme and the use of climatology follow Buijsman et al. (2012) and Uchiyama et al. (2014), with the two innermost domains forced (e.g., via momentum and heat fluxes) with the 6-km-resolution Weather Research and Forecasting Model (Skamarock et al. 2005). For our purposes, ROMS produces plausible surface currents with a horizontal structure at scales smaller than those resolved by the HF radar. The innermost domain encompasses an area larger than the typical medium-range HF radar coverage area (12–13 MHz), with a 100-m-resolution grid. Previous studies used simpler ocean current scenarios, such as a slightly randomized uniform flow (Barrick and Lipa 1996), a current jet (Laws et al. 2000), or radial currents resulting from a large eddy (de Paolo and Terrill 2007). We speculate that the complex radial velocity profiles obtained from ROMS are more representative of the real ocean, and that they provide a realistic and rigorous test of error estimation schemes.

To use the ROMS surface velocity fields, we first compute  $\mathbf{v}_r$  relative to a simulated HF radar site for each ROMS grid point. We then divide the ROMS grid into range cells, each 1.5 km wide containing  $\mathcal{O}(10^3 - 10^4)$ 

Range cell index	Range (km)	No. of grid points	Bearing min	Bearing max	Grid points per degree
3	4	2349	78.6	304.9	10
8	11.5	6139	91.2	295.5	30
20	29.5	15 041	88.3	283.9	77
23	34	16 699	93.7	281.9	89
26	38.5	17 444	95.2	280.4	94
36	53.5	17 067	104.9	253.0	115

TABLE 1. Specifications of ROMS surface currents used in oceanographic radar simulations.

points from the ROMS grid (Table 1), selecting a representative subset of range cells (regions shown in Fig. 2). The total area of each range cell increases with range, such that the number of ROMS grid points within each range cell also increases with range. Variation in the total angular span covered by each range cell, from  $150^{\circ}$  to  $200^{\circ}$ , results in additional variation in the number of ROMS grid points representing each range cell. For example each  $1^{\circ} \times 1.5$ -km HF radar "bin" is resolved by between 10 and 115 grid points (Table 1). Figure 3 shows the profiles of  $\mathbf{v}_r$  obtained from ROMS and used in the radar simulations. Using  $\mathbf{v}_r$  in (8) defines  $\mathbf{X}(t)$  as a function of  $\theta$  and range  $\mathbf{r}$  within the simulated range cell. In this study  $\mathbf{v}_r$  is fixed over the K FFTs.

The factor  $\gamma_{\pm}$  in (8) decorrelates simulated signals, modeling a poorly understood process occurring with ocean backscatter. While signals backscattered from the sea surface originate from a single source (the transmit antenna), it is generally assumed that the signals become decorrelated after scattering from the sea surface, for angular separations as small as  $0.5^{\circ}-2.0^{\circ}$ 

(Lipa and Barrick 1983; Barrick and Lipa 1996). Lipa and Barrick (1983) attribute the value of 0.5° to Barrick and Snider (1977), who estimate decorrelation times (about 25 s) rather than angular separations, and speculate that the mechanism decorrelating the signals is the differential motion of scattering ocean wave trains. Given these unknowns, we decorrelate signals at less than 1° when modeling the backscattered signal. In terms of the direction of arrival estimation, 1° is typically less than the resolution of MUSIC, defining resolution as the "ability... to distinguish between tightly spaced" sources (Friedlander 2009, p. 24). Further discussion of the MUSIC resolution limit is given in appendix B.

To decorrelate simulated signals, we construct  $\gamma_{\pm}$  beginning with an  $N_{\rm v_r} \times 1$  vector of zero mean normally distributed random numbers  $\gamma_{\pm}$ . We then form  $\gamma_{\pm} = {\rm diag}(\gamma_{\pm})$ , resulting in an  $N_{\rm v_r} \times N_{\rm v_r}$  matrix with nonzero values only on the diagonal. We draw new values of  $\gamma_{\pm}$  for each of the K data snapshots, with different values multiplying both the approaching

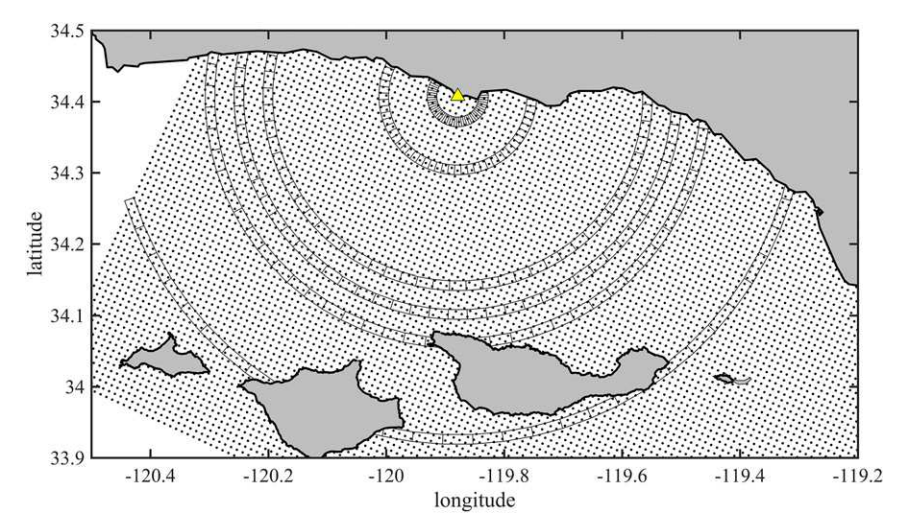


FIG. 2. Simulation domain showing ROMS grid (subsampled to 1 km), along with 1.5-km-wide range cells used for HF radar simulations. The yellow triangle shows the simulated HF radar location, and range cells showing 5° increments are centered on ranges of 4, 11.5, 29.5, 34, 38.5, and 53.5 km. Islands and mainland coast are shown in gray.

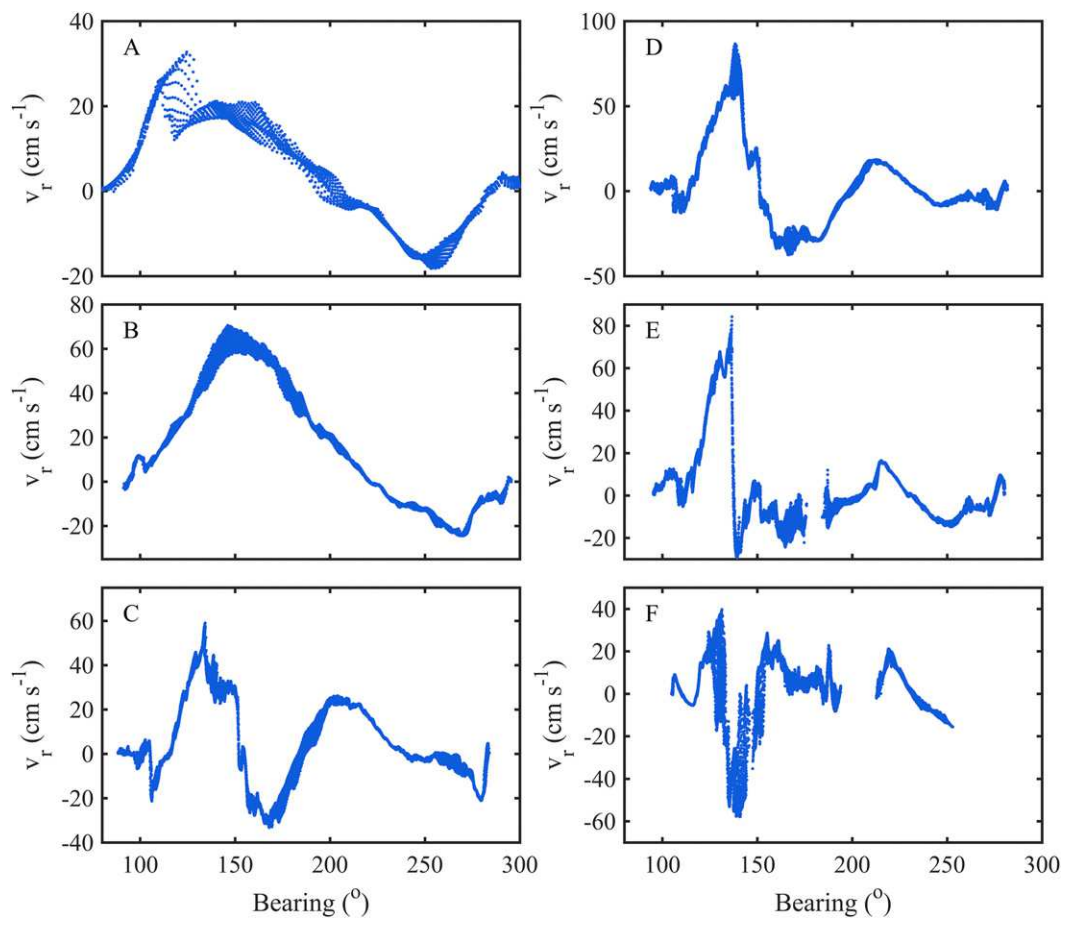


FIG. 3. Radial velocity ( $\mathbf{v}_r$ ) vs bearing from the ROMS, found in 1.5-km-wide range cells: (a) 4, (b) 11.5, (c) 29.5, (d) 34, (e) 38.5, and (f) 53.5 km from a simulated HF radar site as shown in Fig. 2.

 $\gamma_+$  and receding  $\gamma_-$  Bragg peaks separately. Without this randomizing component, the simulation equations present correlated sources of signal. Previous simulation-based studies model wind, assuming a Pierson–Moskowitz cardioid pattern (Pierson and Moskowitz 1964) as a function of  $\theta$  that multiplies  $\bf A$  in (4), with randomness that decorrelates signals in the way that we use  $\gamma_\pm$  (Barrick and Lipa 1996; Laws et al. 2000). Essentially  $\gamma_\pm$  in (8) is equivalent to assuming a uniform presence of Bragg waves, while the use of the Pierson–Moskowitz model for the wave field is equivalent to assuming fully developed seas.

## d. Detecting the number of signal sources

The oceanographic radar simulation [e.g., (4) with (8)] describes a scenario with  $N_{\mathbf{v}_r} \gg M$ , while MUSIC requires N < M. The simulation imitates reality, since operational radars receive signal simultaneously from all directions and from a multitude of Bragg waves. The signal processing (Fig. 1) partially resolves this problem by applying the FFT to the range cell time series

and forming  $\mathbf{C}(f)$  for each Doppler bin, such that  $\mathbf{C}(f)$  considers individual, narrow ranges of  $\mathbf{v}_r$ . Given the density of the ROMS grid however, narrow ranges of  $\mathbf{v}_r$  still contain many point sources. Essentially, the evaluation of (4) and the subsequent signal processing combines similarly valued signal sources (similar in  $\theta$  and  $\mathbf{v}_r$ ) such that these act as spatially cohesive source patches. With respect to MUSIC then, the determination of N becomes the problem of finding the number of spatial patches of similar  $\theta$  and  $\mathbf{v}_r$ .

We determine N for use by MUSIC by inspecting profiles of  $\mathbf{v}_r$ . For example, in Fig. 3a  $\mathbf{v}_r > 25\,\mathrm{cm\,s}^{-1}$  occurs only in the region spanning  $105^\circ-130^\circ$ . For this range of  $\mathbf{v}_r$  we compute MUSIC DOA solutions with N=1. For  $\mathbf{v}_r$  between 5 and  $12\,\mathrm{cm\,s}^{-1}$ , we compute MUSIC solutions with N=2. Velocities between -1 and  $6\,\mathrm{cm\,s}^{-1}$  occur at three distinct bearings. In this case we compute MUSIC with N=2 (as required by the N < M limitation) and label these as N=3. Thus, the profiles of  $\mathbf{v}_r$  require some interpretation for determining N, as the criterion for what constitutes a

spatially distinct source patch is somewhat subjective. However, this method of determining N for MUSIC allows us to partition the results based on N as presented by the simulated ocean current. Ideally, this method also removes signal detection as a significant source of error.

## 4. Analytical DOA uncertainty expressions

Stoica and Nehorai (1989) derive an expression for the MUSIC DOA error variance, based on the statistical properties of the errors in the eigenvectors of  $\mathbf{C}$ . Beginning with the M eigenvalues of  $\mathbf{C}, \lambda_1, \ldots, \lambda_M$ , we associate the largest N with the signal and form the  $M \times N$  matrix of signal eigenvectors  $\mathbf{S} = [\mathbf{s}_1, \ldots, \mathbf{s}_N]$ . We then associate the remaining M - N eigenvectors with the noise and form the  $M \times (M - N)$  matrix  $\mathbf{G} = [\mathbf{g}_1, \ldots, \mathbf{g}_{M-N}]$ . The MUSIC error variance of the ith DOA is then given by

$$\sigma_{\text{MU}}^2 = \frac{1}{2K} \frac{\mathbf{a}^H(\theta_i) \mathbf{U} \mathbf{a}(\theta_i)}{h(\theta_i)}, \tag{9}$$

where **U** is defined as

$$\mathbf{U} = \sigma^2 \left[ \sum_{k=1}^{N} \frac{\lambda_k}{(\sigma^2 - \lambda_k)^2} \mathbf{S}_k \mathbf{S}_k^H \right], \tag{10}$$

and  $h(\theta_i)$  is given by

$$h(\theta_i) = \frac{d\mathbf{a}(\theta_i)^H}{d\theta} \mathbf{G} \mathbf{G}^H \frac{d\mathbf{a}(\theta_i)}{d\theta}, \tag{11}$$

given the noise variance  $\sigma^2$  (units:  $V^2$ ), the receive array vector  $\mathbf{a}(\theta)$ , and its derivative with respect to  $\theta$  (see appendix B for derivative calculation methods). As the eigenvalues approach the noise variance, the denominator in (10) goes to zero, or  $(\sigma^2 - \lambda_k) \to 0$ , and the MUSIC error variance becomes large. The expressions (9)–(11) produce estimates of the error variance in radians squared. The DOA uncertainty  $\sigma_{\text{MU}}$  is then the positive square root of (9) converted into degrees.

#### 5. Results

### a. Discrete source simulations

To investigate the SeaSonde DOA errors in a simplified scenario, we performed simulations of two sources located at  $\theta_1 = -22.5^{\circ}$  and  $\theta_2 = 22.5^{\circ}$  using the discrete source model (7) with (4). Figure 4 summarizes the results, showing the RMS difference  $\sigma_{\rm RMS}$  [computed with (B6)] between the source locations  $\theta_N$  and the MUSIC DOA solutions  $\theta_{\rm MU}$ , computed in 2-dB SNR bins and plotted versus SNR. For SNR between 15 and 25 dB,  $\sigma_{\rm RMS}$  ranges from 5° to 10°, comparable to

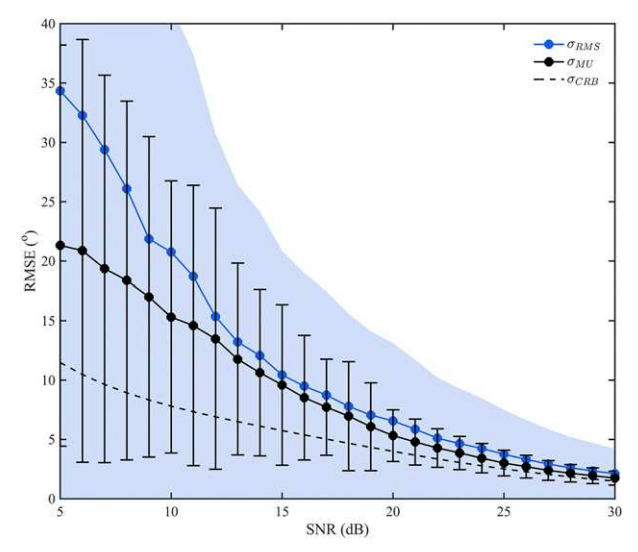


FIG. 4. Results from simulations of two discrete source signals received with the SeaSonde [computed using (4) with (7)]. The figure shows the RMS error ( $\sigma_{\rm RMS}$ , blue dots) between the simulated signal source bearing ( $\theta_{\rm N}$ ) and the DOA solutions ( $\theta_{\rm MU}$ ). Mean values of the error estimates ( $\sigma_{\rm MU}$ , black dots) computed with (9) from Stoica and Nehorai (1989) are also shown. Dashed line shows the Cramer–Rao lower bound ( $\sigma_{\rm CRB}$ ) computed with (B5). Light blue shading indicates  $\pm 1$  standard deviation of the DOA errors ( $\theta_{\rm N}-\theta_{\rm MU}$ ), while black error bars indicate  $\pm 1$  standard deviation of the  $\sigma_{\rm MU}$  estimates. Calculations use 2-dB-wide SNR bins.

the low end of published bearing errors found in observations (2°–30°) (Emery et al. 2004; Paduan et al. 2006; Liu et al. 2010; Lorente et al. 2014; Lai et al. 2017a). Standard deviations of the DOA errors (blue shaded area) illustrate the spread in the data from which the  $\sigma_{\rm RMS}$  are computed.

Figure 4 also shows the estimates of the DOA uncertainty ( $\sigma_{\text{MU}}$ ) computed with (9). We plot average values of  $\sigma_{\text{MU}}$  found in each 2-dB SNR bin, since distinct values of  $\sigma_{\text{MU}}$  are produced with each  $\theta_{\text{MU}}$ . The figure demonstrates that mean  $\sigma_{\text{MU}}$  track  $\sigma_{\text{RMS}}$  for SNR  $\geq$  12 dB, underestimating  $\sigma_{\text{RMS}}$  by 1°–2°. Error bars on  $\sigma_{\text{MU}}$ , showing the bin standard deviations, have a narrower range than the DOA error standard deviations, suggesting a limitation of the  $\sigma_{\text{MU}}$  estimate.

Figure 4 includes the Cramer–Rao Bound  $\sigma_{CRB}$ , which gives the theoretical lower bound on estimation error based solely on the APM, the SNR, and the number of signal sources (Stoica and Nehorai 1989; Friedlander 2009) (see appendix B for its calculation). For SNR <15, the difference between  $\sigma_{RMS}$  and  $\sigma_{CRB}$  becomes substantial, suggesting the possibility of obtaining decreased  $\sigma_{RMS}$  with the use of a different DOA estimator. For SNR > 25 dB,  $\sigma_{MU}$  and  $\sigma_{RMS}$  approach  $\sigma_{CRB}$ , illustrating that 1) MUSIC achieves near-optimal

performance for the SeaSonde in this SNR range; 2) the theoretical minimum on the SeaSonde DOA error is around 2°; and 3) the lowest error is achieved at the highest SNR.

Simulations with the discrete source model and the results in Fig. 4 establish the fundamental performance of both the SeaSonde array and the DOA uncertainty estimates given by  $\sigma_{\rm MU}$ . That these results depend only on the ideal SeaSonde antenna patterns, variable SNR, and two signal sources suggests that these factors are responsible for a significant fraction of the DOA error variance. These results reproduce the overall behavior of much more complex simulations (e.g., Fig. 6b below), showing the value of the discrete source model for investigating these aspects of the HF radar processing.

## b. Oceanographic radar simulations

Beginning with the ranges cells of  $\mathbf{v}_r$  obtained from ROMS (e.g., Fig. 3), we simulated voltages received on the SeaSonde array with (4) and (8) and processed these as described in section 2. For each 2-dB SNR increment in the interval 6-36 dB, we ran 400 Monte Carlo simulations. Figure 5 shows the results of one simulation with SNR  $\sim$ 20 dB, with DOA solutions ( $\theta_{MU}$ ) plotted over the input ocean current  $(\mathbf{v}_r)$  from ROMS (blue dots). In this example, we use single-bearing solutions (N = 1) in the MUSIC calculation for  $\mathbf{v}_r > 57 \,\mathrm{cm \, s}^{-1}$  and  $\mathbf{v}_r < -12 \,\mathrm{cm \, s}^{-1}$ , three-bearing solutions (N=3) for  $\mathbf{v}_r$ between 0 and  $-10 \,\mathrm{cm \, s}^{-1}$ , and dual-bearing solutions (N = 2) for the remainder. Error bars on  $\theta_{MU}$  show the bearing uncertainties  $\pm \sigma_{\rm MU}$  estimated with (9). For the N = 1 case, the DOA solutions fall within ROMS  $\mathbf{v}_r$ , with correspondingly low  $\sigma_{MU}$ . Many of the N=2 DOA solutions fall outside the range of bearings spanned by  $\mathbf{v}_r$ , though the greater  $\sigma_{\mathrm{MU}}$  associated with these often includes  $\mathbf{v}_r$ . The N=3 case illustrates how the presence of signals from a third bearing biases the MUSIC DOAs, with some falling between areas of  $\mathbf{v}_r$  (e.g., near  $\sim 250^\circ$ ). These simulation results suggest that  $\sigma_{MU}$  provides a useful indicator of error.

Results of the radar simulations with ROMS are summarized by computing the  $\sigma_{\rm RMS}$  between the source  $\theta_N$  and the MUSIC  $\theta_{\rm MU}$ , in 2-dB-wide SNR bins. As described in the appendix,  $\sigma_{\rm RMS}$  is computed between  $\theta_{\rm MU}$  and the  $\theta_N$  from the nearest  ${\bf v}_r$  in bearing. Figure 6 shows the results of these calculations, plotting  $\sigma_{\rm RMS}$  versus SNR, with the results partitioned by the N empirically determined from the input ocean current field.

Figure 6a shows the results for N = 1, with  $\sigma_{\rm RMS} < 5^{\circ}$  for SNR > 10 dB. The results in Fig. 6b with N = 2 show increased  $\sigma_{\rm RMS}$  over the N = 1 case, particularly in the SNR range of 10–25 dB, where  $\sigma_{\rm RMS}$  is more than double that for N = 1. These results are similar to Fig. 4,

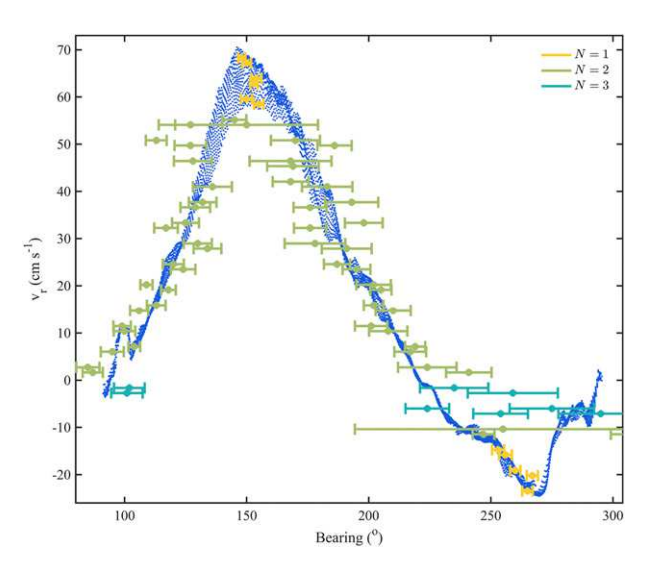


FIG. 5. Radial velocity vs bearing from the ROMS (blue dots; also shown in Fig. 3b), found in a 1.5-km-wide range cell, 11.5 km from a simulated HF radar site. The figure shows example DOA solutions (dots) and  $\pm \sigma_{\rm MU}$  (error bars) for N=1, 2, and 3, from a simulation with a maximum SNR of 20 dB.

though with narrower bin standard deviations of  $\theta_N - \theta_{\text{MU}}$  (blue shading). Figure 6c with N=3 shows  $\sigma_{\text{RMS}}$  consistently near 15°, showing the influence of the additional signal source (i.e., N=M) on the MUSIC calculation. Overall,  $\sigma_{\text{RMS}}$  increases with increasing N, as shown by curves of  $\sigma_{\text{RMS}}$  in Figs. 6a–c. Figures 6a and 6b also demonstrate the relationship between SNR and error, which breaks down for N=3 (Fig. 6c).

Figure 6 shows the mean of  $\sigma_{\text{MU}}$  found in 2-dB SNR bins, along with the standard deviation. In both the N=1 and N=2 cases, Figs. 6a and 6b,  $\sigma_{\text{MU}}$  tracks  $\sigma_{\text{RMS}}$ , providing a reasonable estimate of the observed RMS error. However, Fig. 6c suggests that mean  $\sigma_{\text{MU}}$  underestimates  $\sigma_{\text{RMS}}$  when SNR >10 dB and N=3. In Fig. 6c, mean  $\sigma_{\text{MU}} \approx 8^{\circ}$  is found at relatively high SNR, while in the N=1 and N=2 cases these values of mean  $\sigma_{\text{MU}}$  are found only at low SNR. In each example, mean  $\sigma_{\text{MU}} \geq 8^{\circ}$  corresponds to relatively high  $\sigma_{\text{RMS}}$ . This observation, along with the correspondence between  $\sigma_{\text{MU}}$  and  $\sigma_{\text{RMS}}$ , otherwise suggests the use of  $\sigma_{\text{MU}}$  as a metric for thresholding.

## c. Application to operational radars

Uncertainty estimates were also evaluated by processing spectra from two SeaSondes, located at Santa Cruz Island, California (SCI1), and San Nicolas Island, California (SNI1), using software we developed (Emery 2018). Starting with unaveraged SeaSonde spectra files (CSQ), the software follows the methods and conventions of the SeaSonde processing scheme (e.g., Fig. 1). Rather than running the DOA processing on 10-min

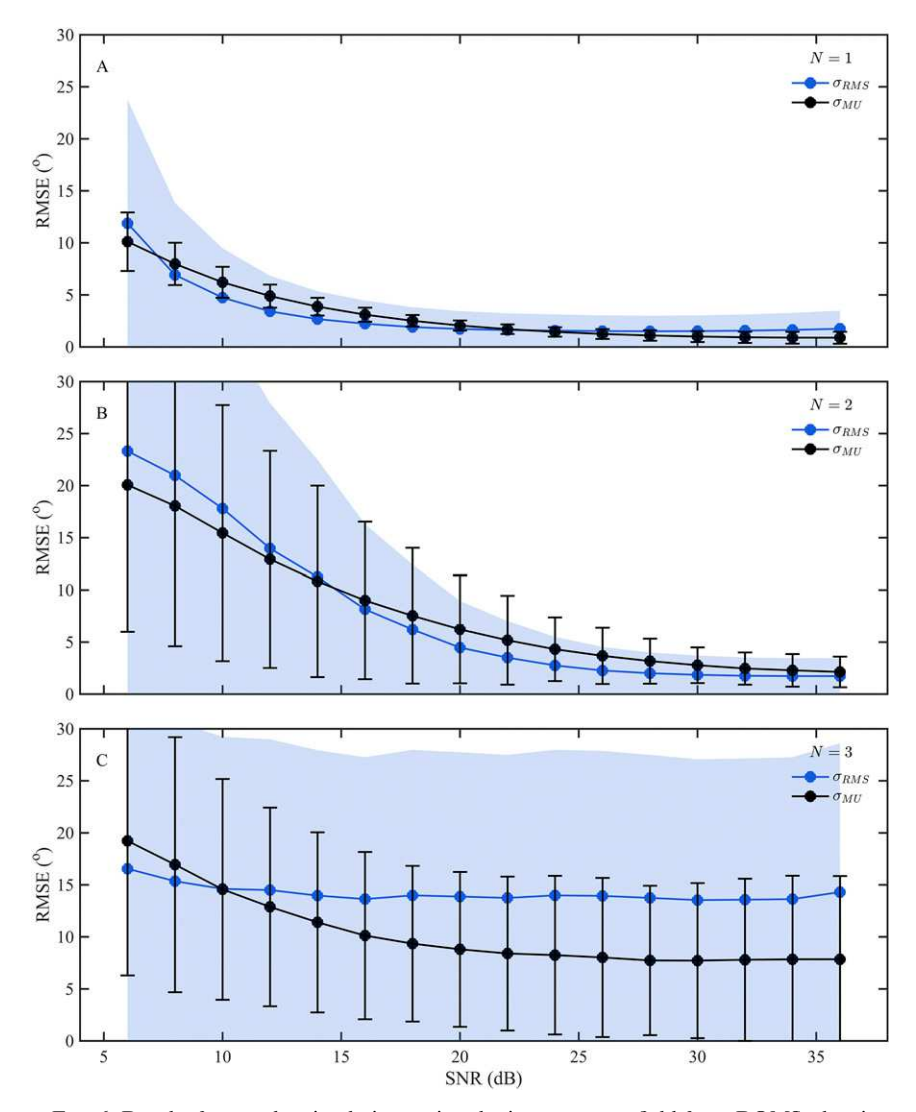


FIG. 6. Results from radar simulations using the input current field from ROMS, showing  $\sigma_{\rm RMS}$  and the mean of the estimated errors  $\sigma_{\rm MU}$ , when the same velocity is present: (a) at a single bearing (N=1), (b) at two bearings (N=2), and (c) at three bearings (N=3). Blue shaded regions show  $\pm 1$  standard deviation of the bin DOA errors, while the black error bars show  $\pm 1$  standard deviation of the bin  $\sigma_{\rm MU}$  estimates.

moving averages of auto- and cross-spectra, as is typical for SeaSonde processing, we computed moving averages of 16 auto- and cross-spectra every 10 min. Since each power spectrum results from 256s of data, the average covers 68.3 min. The software also uses the First Order Line (FOL) toolbox (Kirincich 2017) for first-order region identification. Antenna patterns were obtained for both sites using the methods of Emery et al. (2014) with two months of data.

Figure 7 shows time series of  $\mathbf{v}_r$  from near the baseline between SCI1 and SNI1, for the interval 10–12 August 2013. The plots show  $\mathbf{v}_r$  every 10 min from the spatial area within  $\pm 1^\circ$  in bearing and  $\pm 3$  range cells of the

midpoint between the sites for a total of 21 locations on each radial grid. Vertical bars at each velocity observation show the  $\sigma_{\rm MU}$  error estimate in degrees. In general, smaller  $\sigma_{\rm MU}$  occurs when  ${\bf v}_r$  falls into groups, suggesting that the repeatable observations of  ${\bf v}_r$  have lower DOA errors. Based on inspection of the cross-spectra, observations of  ${\bf v}_r$  near 100 cm s<sup>-1</sup> in Fig. 7a result from ship backscatter. Figure 7 and Table 2 show sight differences in mean and median  $\sigma_{\rm MU}$  from the two sites. Slightly lower mean and median  $\sigma_{\rm MU}$  from SCI1 correspond to the slightly higher SNR observed there.

Figure 8 shows the spatial distribution of  $\sigma_{MU}$ , averaged over 10–20 August 2013. The figure shows a wide

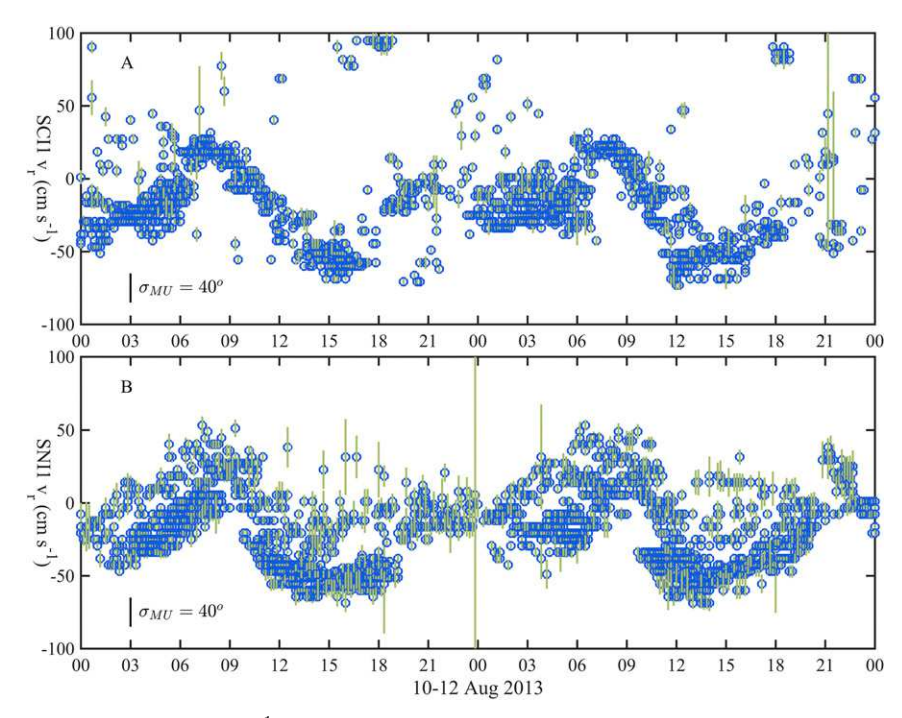


FIG. 7. Plots of  $\mathbf{v}_r$  (cm s<sup>-1</sup>) vs time with  $\sigma_{\rm MU}$  (°) for HF radars at (a) Santa Cruz Island and (b) San Nicolas Island at 10-min intervals from 0000 UTC 10 Aug to 0000 UTC 12 Aug 2013.

range of average values, along with high values found at particular bearings, indicating a dependence on the APM. Only a fraction of the observations have  $\sigma_{\text{MU}} > 10^{\circ}$  for these two HF radars (SCI: 10.5%; SNI: 7.1%; Table 2). The prevalence of high values of  $\sigma_{\text{MU}}$  in Fig. 8 and the outlier  $\mathbf{v}_r$  in Fig. 7 with high values of  $\sigma_{\text{MU}}$  further suggest the use of  $\sigma_{\text{MU}}$  as a quality control metric.

Using the near-baseline data described for Fig. 7, we compute the RMS difference (RMSD) and  $r^2$  between the two time series, varying the threshold value of  $\sigma_{\rm MU}$  for removing data. Figure 9 shows  $r^2$  and RMSD, versus the threshold value of  $\sigma_{\rm MU}$  along with the 95% confidence intervals. The comparison statistics improve for small values of the  $\sigma_{\rm MU}$  threshold. Figure 9 suggests that removing all but the lowest error data will provide the best comparison. Similar results were found using slightly smaller and slightly larger overlapping spatial areas. We interpret the Fig. 9 results as an indication that the  $\sigma_{\rm MU}$  estimates contain useful information about the DOA uncertainty.

Table 2. Statistics of  $\sigma_{\rm MU}$  as computed for each HF radar site over 10–20 Aug 2013.

Site	σ <sub>MU</sub>	σ <sub>MU</sub> std	σ <sub>MU</sub>	% of $\sigma_{\rm MU}$	Data
	mean (°)	dev (°)	median (°)	> 10°	points
SCI	2.7	6.9	2.0	10.5	8058
SNI	3.8	13.2	2.7	7.1	8784

#### 6. Discussion

Both  $\sigma_{\rm MU}$  and  $\sigma_{\rm CRB}$  illuminate factors controlling error in the DOA of oceanographic radars. Taken together,  $\sigma_{CRB}$  and  $\sigma_{MU}$  show that error in the DOA estimate depends on K, the SNR, the specific receive array, its antenna pattern, and the derivative of the antenna pattern with respect to  $\theta$ . Though not explicit in the expression for  $\sigma_{MU}$ , the number of array elements (M) implicitly factors into the DOA error and  $\sigma_{\rm MU}$  estimate (Stoica and Nehorai 1989; Lai et al. 2017b). The dependence on M, and thus array design, implies different theoretical accuracies for different arrays. While our results are specific to SeaSonde HF radars, we have performed numerous evaluations of  $\sigma_{\rm MU}$  with simulations involving different receive arrays. Simulationbased experiments, using both 16-element linear arrays and 8-element rectangular grid arrays, thus far suggest that  $\sigma_{\rm MU}$  substantially underestimates  $\sigma_{\rm RMS}$  for these radars. These results may confirm the importance of the bias term in computing DOA error (Xu and Buckley 1992), particularly for arrays with M > 3. The bias term appears to be very small or zero when N = M - 1.

The complex currents obtained from ROMS often present the same velocity at more N than there are M, such that often  $N \ge M$  (as stated above, MUSIC is limited to identifying N < M bearings). When  $N \ge M$ ,

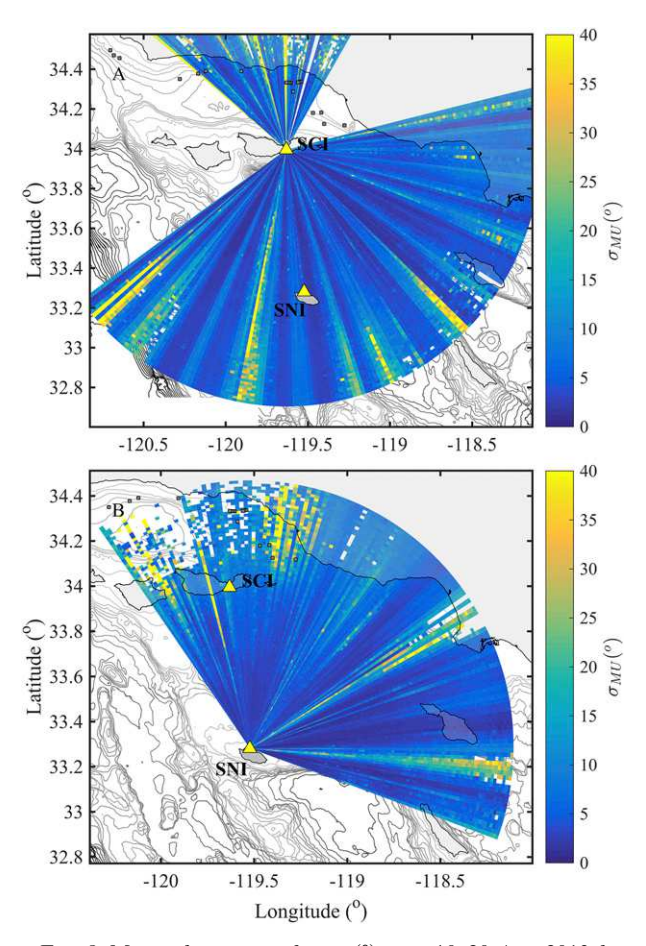


FIG. 8. Maps of average of  $\sigma_{MU}$  (°) over 10–20 Aug 2013 for HF radars at (a) Santa Cruz Island and (b) San Nicolas Island. Both maps show a section of the Southern California Bight, with bathymetry (black lines), islands, and the mainland (gray regions).

MUSIC is unable to partition the signal and noise subspaces (Krim and Viberg 1996; Abramovich et al. 2009), causing a corruption of the noise subspace. This causes an increase in the MUSIC DOA errors—errors that appear to be captured by  $\sigma_{\rm MU}$ . For SeaSondes with M=3, results suggest that while  $\sigma_{\rm MU}$  may not approximate the errors when the current field presents N>2 (e.g., Fig. 6), the  $\sigma_{\rm MU}$  values that result are large in the mean and thus provide a useful uncertainty metric.

Systems using larger numbers of antennas, such as with M = 8 or M = 16, would encounter the problem of  $N \ge M$  less often. The ability of these systems to resolve more flow complexity when using direction of arrival methods such as MUSIC instead of beamforming has been demonstrated (Sentchev et al. 2013). With a few exceptions (e.g., Barbin et al. 2006; Forget et al. 2008; Molcard et al. 2009; Orfila et al. 2015), oceanographic systems with  $M \ge 8$  typically use beamforming

techniques that negate the possibility of within beamwidth resolution.

This analysis suggests that the DOA method is a major source of random error in oceanographic radar ocean current observations. When combined with other sources of error (e.g., Fig. 1), these may explain the intrinsic noise found previously in HF radar data by looking at the power spectral density of HF radar time series (Emery et al. 2004; Forget 2015). In a detailed investigation of the noise properties of WERA HF radar using MUSIC, Forget (2015) showed that even with outlier removal an inherent noise persists, reducing the effective temporal resolution. Random bearing errors resulting from the DOA method (MUSIC in both cases) certainly contribute to—if not fully explain—the reported noise level. The occurrence of  $N \ge M$ , or errors resulting from the determination of N, may also contribute.

#### 7. Conclusions

We evaluate an analytical approach given by Stoica and Nehorai (1989) for estimating  $\sigma_{\rm MU}$  along with the direction measured by SeaSonde oceanographic HF radars. By simulating the backscattered signals from a realistic example of the ocean surface currents, we show that  $\sigma_{\rm MU}$  track errors in the DOAs produced by MUSIC. We also compute  $\sigma_{\rm MU}$  for two operational SeaSonde HF radars, producing mean  $\sigma_{\rm MU}$  values of 2.7° (SCI) and 3.8° (SCI). Results from these HF radars show improved comparison statistics along an overwater baseline when using  $\sigma_{\rm MU}$  as an error threshold for eliminating  $\mathbf{v}_r$  with large bearing errors.

Expressions from Stoica and Nehorai (1989) give bearing uncertainty estimates associated with each radial velocity. These estimates enable the mapping of uncertainty and enable the calculation of the error covariance among surface current observations. Oceanographic HF radar processing schemes, such as the SeaSondes, accurately estimate the radial current speed, but they less accurately estimate the bearing to the patch of ocean surface where the radial speed occurs. Given this property of data from individual HF radars, algorithms used to form the total vector velocities should account for bearing uncertainties. Further work remains to propagate the spatial uncertainty estimate provided by  $\sigma_{MU}$  to the total velocity vector, but it is expected that the uncertainty estimates will be useful for assimilating HF radar data into numerical models of ocean circulation.

These results along with previous results from the literature cited above outline the primary sources of error for oceanographic HF radars. The analysis supports the following for the quantification of uncertainty

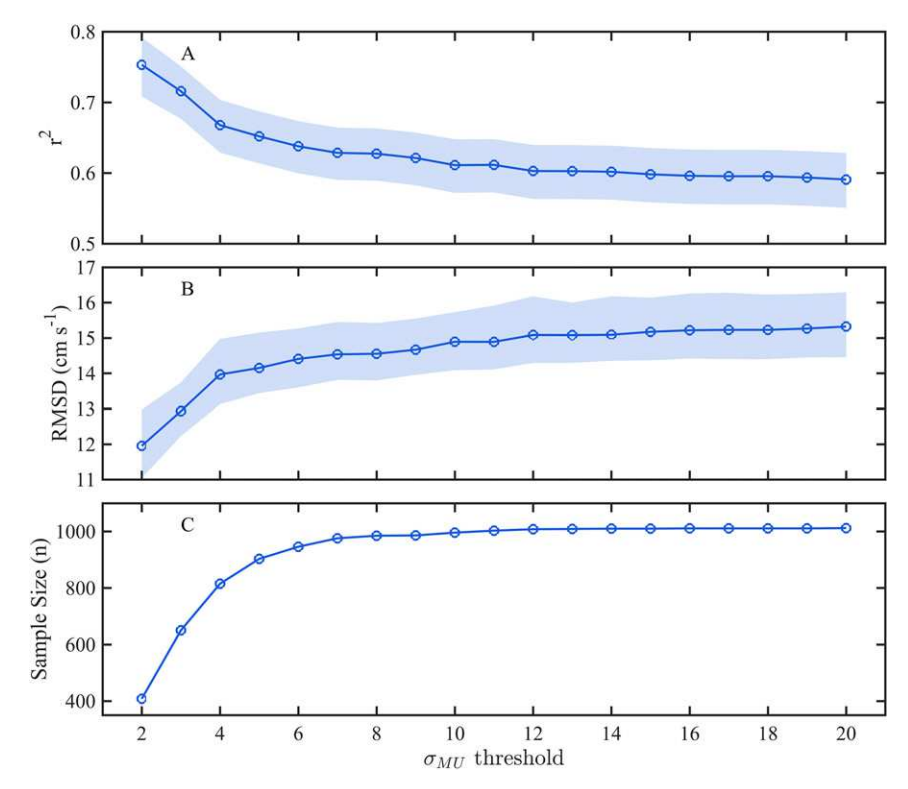


FIG. 9. Comparison statistics between velocities measured at SCI1 and SNI1 in a region of overlapping coverage along the baseline, computed after thresholding with  $\sigma_{\text{MU}}$ : (a)  $r^2$  and (b) RMSD, and (c) sample size. Shaded region shows the 95% confidence interval, with the interval in (b) obtained with bootstrap sampling (Efron and Tibshirani 1994).

in the radial velocity components of oceanographic radars:

$$\mathbf{v}_{r}(r,\theta) = \mathbf{v}_{r}(r \pm \sigma_{r}, \theta \pm \sigma_{\theta}) \pm \sigma_{\mathbf{v}}, \qquad (12)$$

where (1) provides an estimate for the range uncertainty  $\sigma_r$ , (2) provides an estimate for the bin velocity uncertainty  $\sigma_{v_r}$ , and (9) provides the estimate for the bearing uncertainty  $\sigma_{\theta}$  when using MUSIC. Errors resulting from interfering signals, improper determination of the first-order region, or imperfect knowledge of the antenna pattern are not quantified by (12). Estimating the contribution from these additional components of error and the identification of a general method for estimating errors in data from all oceanographic radars are the subjects of ongoing work.

Acknowledgments. The authors thank D. Barrick, C. Whalen, and B. Rector of CODAR Ocean Sensors Ltd. for providing the software from which simulations were derived, as well as for the helpful related discussions. We thank L. Romero for the ROMS data. This work was supported by the National Science Foundation under Grant OCE-1658475. Computing resources were provided by the UCSB Center for Scientific Computing

[NSF MRSEC (DMR-1720256) and NSF CNS-1725797]. Any opinions, findings, and conclusions or recommendations expressed in this material are those of the authors and do not necessarily reflect the views of the National Science Foundation.

## APPENDIX A

# **Mathematical Symbols**

The definition of each mathematical symbol is defined in Table A1.

### APPENDIX B

#### Calculation Details

#### a. MUSIC resolution limit

The MUSIC resolution limit, defined as the ability to distinguish closely spaced signal sources, is approximated by

$$\Delta \theta = \theta_{\text{HPBW}} \text{SNR}^{-1/p}, \qquad (B1)$$

TABLE A1. Definitions of symbols used in the manuscript.

Symbol	Definition		
A	Matrix of receive array vectors		
$\mathbf{a}(\theta)$	Receive array vector		
В	Beam pattern		
<b>C</b> ( <i>f</i> )	Data covariance matrix at Doppler		
• /	frequency f		
$\mathbf{C}_{y}$	Estimate of covariance matrix		
c	Speed of light		
$\Delta \mathbf{r}$	Range cell width (km)		
$\Delta \mathbf{v}_r$	Radar radial velocity increment (cm s		
$\mathbf{e}(t)$	Noise time series		
$f_{\mathrm{TX}}$	Radar transmit frequency		
g	Gravitational acceleration		
Ğ	Matrix of noise eigenvectors $\mathbf{g}_{M-N}$		
$oldsymbol{\gamma}_{\pm}$	Decorrelation factor		
K	No. of data snapshots (e.g., No. of		
	spectra averaged together)		
$k_{\mathrm{TX}}$	Radar wavenumber		
$\lambda_M$	Eigenvalues of $\mathbf{C}(f)$		
$\lambda_{\mathrm{TX}}$	Wavelength of transmitted radio wave		
M	No. of receive antennas		
N	No. of signal sources or signal source bearings		
n	No. of data points in $\sigma_{RMS}$ calculation, or sample size		
$N_{\mathbf{v}_r}$	Length of the vector $\mathbf{v}_r$		
$n_{\mathrm{FFT}}$	Length of the time series for FFT processing		
r	Range (km)		
s	Matrix of signal eigenvectors $\mathbf{s}_N$		
$\sigma^2$	Noise variance		
$\sigma_{ m CRB}$	Cramer–Rao lower bound on DOA error		
$\sigma_{ m MU}$	DOA error estimated with (9)		
$\sigma_{ m RMS}$	DOA RMS error		
$\sigma_{ m r}$	Range uncertainty (km)		
$\sigma_{\mathbf{v}_r}$	Radial velocity uncertainty (cm s <sup>-1</sup> )		
$\theta$	Direction from radar to signal source		
$\theta_N$	Direction from radar to Nth signal source		
$\theta_{ m HPBW}$	Half-power beamwidth		
$ heta_{ m MU}$	DOA solution from MUSIC (MUSIC		
• МО	estimate of $\theta_N$ )		
$\mathbf{v}_r$	Radar radial velocity component (cm s <sup>-1</sup> )		
$\pm \omega_B$	Frequency shift due to Bragg resonant waves		
$\boldsymbol{\omega}_c$	Frequency shift resulting from ocean currents		
$\mathbf{X}(t)$	Signal source time series		
Y	Receive antenna voltage time series matrix		

where p ranges between 2 and 4 (Friedlander 2009; Amar and Weiss 2007), and  $\theta_{HPBW}$  is the half-power beamwidth. To estimate  $\Delta\theta$  we compute  $\theta_{HPBW}$  by first computing the beam pattern **B** following Van Trees (2002),

$$\mathbf{B} = \frac{1}{M} \mathbf{A} (\theta_o)^H \mathbf{A} (\theta), \tag{B2}$$

where  $\theta_o$  is a reference angle, and then finding  $\theta_{\rm HPBW}$  as the range of  $\theta$ , where  $|\mathbf{B}|^2 \ge 0.5 \text{max} |\mathbf{B}|^2$  (Van Trees 2002). Defined this way, the SeaSonde  $\theta_{\rm HPBW} = 131^\circ$ , while a

uniform linear array (ULA) with  $1/2\lambda_{TX}$  spacing and M=16 has  $\theta_{HPBW}=6.5^{\circ}$ . These values suggests a minimum  $\Delta\theta$  on the order of  $10^{\circ}-20^{\circ}$  for the SeaSonde (with SNR = 30 dB and p=2 or p=4). Using data we processed from SeaSondes (which has the individual MUSIC DOA solutions), we plotted the angular difference between dual-bearing solutions versus SNR (not shown), indicating a minimum  $\Delta\theta$  on the order of  $10^{\circ}$ . For the purposes of simulating ocean current backscatter, these results suggest that decorrelating sources separated by  $<1^{\circ}$  adequately approximates backscatter from the ocean surface.

#### b. Cramer-Rao lower bound

In addition to estimates of  $\sigma_{\rm MU}$ , we compute the Cramer–Rao bound (CRB) on DOA error variance following Stoica and Nehorai (1989) and Friedlander (2009). Here we use its square root  $\sigma_{\rm CRB}$  to illustrate factors controlling the DOA error, to compare with uncertainties estimated with (9), and to compare with simulation results. We compute  $\sigma_{\rm CRB}$  from the antenna pattern  ${\bf a}(\theta)$  and from assumed values of SNR, K, and N. Following Friedlander (2009) we estimate a covariance matrix  ${\bf C}_y$  directly from these known variables, along with the identity matrix  ${\bf I}$ ,

$$\mathbf{C}_{y} = \sum_{k=1}^{N} SNR_{k} \mathbf{a}(\theta_{k}) \mathbf{a}(\theta_{k})^{H} + \mathbf{I}.$$
 (B3)

We then define the (i, j)th element of the  $N \times N$  Fisher information matrix,

$$\mathbf{F}_{i,j} = \operatorname{trace} \left[ \mathbf{C}_{y}^{-1} \frac{\partial \mathbf{C}_{y}}{\partial \theta_{i}} \mathbf{C}_{y}^{-1} \frac{\partial \mathbf{C}_{y}}{\partial \theta_{i}} \right]. \tag{B4}$$

From **F** the CRB is given by

$$\sigma_{\text{CRB}}^2 \ge \frac{1}{K} \mathbf{F}^{-1} \equiv \text{CRB}.$$
 (B5)

Calculation of the derivative of  $\mathbf{C}_y$  with respect to  $\theta$  in (B4) is described below. As defined above  $\sigma_{CRB}$  applies to the estimation of DOA uncertainties for discrete signal sources.

## c. Simulation DOA errors

We compute errors in the DOA estimates as the RMS difference between the simulated source bearing  $\theta_N$  and  $\theta_{\text{MU}}$ . We compute the  $\sigma_{\text{RMS}}$  for a given ensemble of n DOA solutions as

$$\sigma_{\text{RMS}} = \sqrt{\frac{\sum_{i=1}^{n} \left(\theta_{N_i} - \theta_{\text{MU}_i}\right)^2}{n}}.$$
 (B6)

A typical ensemble includes all points within a given range of SNR. For discrete source simulations with the source  $\theta$  specified, calculation of (B6) is straightforward. However, when computing  $\sigma_{\rm RMS}$  for simulations using ROMS, the calculation is more complex. In this case, a DOA solution  $\theta_{\rm MU}$ , associated with a given  $\mathbf{v}_r$ , results from a signal that may originate from a wide range of bearings. For example, the radial currents in Fig. 3a have  $\mathbf{v}_r = 10\,\mathrm{cm\,s^{-1}}$  for bearings between 95°–100° and  $160^\circ$ –185°, meaning that  $\theta_N$  can take on any value in these ranges. When computing the error with a DOA solution  $\theta_{\rm MU}$ , we retain the smallest difference  $\theta_{N_i} - \theta_{\rm MU_i}$  for use in (B6), using the value of  $\theta_N$  from the current field that is closest to the DOA solution.

#### d. Derivative calculations

Assuming an ideal pattern for SeaSondes, the array derivative in (11) can be evaluated analytically, but for APMs from operational radars we must evaluate the array derivative numerically. We compute these derivatives using the second-order accurate centered difference:

$$\frac{da(\theta_j)}{d\theta} = \frac{a(\theta_{j+1}) - a(\theta_{j-1})}{2\Delta\theta}.$$
 (B7)

Edges are evaluated using the first-order accurate forward and backward one-sided approximations (LeVeque 2007):

$$\frac{da(\theta_1)}{d\theta} = \frac{a(\theta_2) - a(\theta_1)}{\Delta\theta},$$
 (B8)

$$\frac{da(\theta_n)}{d\theta} = \frac{a(\theta_n) - a(\theta_{n-1})}{\Delta \theta}.$$
 (B9)

We compute the derivative of  $\mathbf{C}_y$  with respect to  $\theta$  in (B4) as in Friedlander (2009),

$$\frac{\partial \mathbf{C}_{y}}{\partial \theta_{i}} = \text{SNR}_{i} \frac{d\mathbf{a}(\theta_{i})}{d\theta} \mathbf{a}(\theta_{i})^{H} + \text{SNR}_{i} \mathbf{a}(\theta_{i}) \frac{d\mathbf{a}(\theta_{i})^{H}}{d\theta}.$$
(B10)

The array derivatives are computed as described above.

#### REFERENCES

- Abramovich, Y. I., B. A. Johnson, and X. Mestre, 2009: DOA estimation in the small-sample threshold region. *Classical and Modern Direction-of-Arrival Estimation*, T. E. Tuncer and B. Friedlander, Eds., Academic Press, 219–287, https://doi.org/10.1016/B978-0-12-374524-8.00006-4.
- Amar, A., and A. J. Weiss, 2007: Resolution of closely spaced deterministic with given success rate signals. *Proceedings: 2007 IEEE International Symposium on Information Theory*, IEEE, 1791–1795, https://doi.org/10.1109/ISIT.2007.4557481.
- Barbin, Y., P. Broche, J. de Maistre, P. Forget, and J. Gaggelli, 2006: Practical results of Direction Finding method applied

- on a 4 antenna linear array WERA. *Proc. Sixth Int. Workshop on Radio Oceanography (ROW-6)*, Hamburg, Germany, Universität Hamburg, http://wera.cen.uni-hamburg.de/ROW\_2006/Abstract\_Barbin\_2.shtml.
- Barrick, D. E., and J. B. Snider, 1977: The statistics of HF sea-echo Doppler spectra. *IEEE J. Oceanic Eng.*, **2**, 19–28, https://doi.org/10.1109/JOE.1977.1145317.
- —, and B. J. Lipa, 1996: Comparison of direction-finding and beamforming in HF radar ocean surface current mapping. NOAA Phase 1 SBIR Final Rep., Contract 50-DKNA-5-00092, 81 pp.
- —, and —, 1999: Radar angle determination with MUSIC direction finding. U.S. Patent 5,990,834, filed 29 August 1997, and issued 23 November 1999.
- Bendat, J. S., and A. G. Piersol, 2000: Random Data: Analysis and Measurement Procedures. 3rd ed. Wiley Series in Probability and Statistics, 594 pp.
- Buijsman, M., Y. Uchiyama, J. McWilliams, and C. Hill-Lindsay, 2012: Modeling semidiurnal internal tide variability in the Southern California Bight. *J. Phys. Oceanogr.*, **42**, 62–77, https://doi.org/10.1175/2011JPO4597.1.
- Chapman, R. D., and H. C. Graber, 1997: Validation of HF radar measurements. *Oceanography*, 10 (2), 76–79, https://doi.org/ 10.5670/oceanog.1997.28.
- —, L. Shay, H. C. Graber, J. Edson, A. Karachintsev, C. Trump, and D. Ross, 1997: On the accuracy of HF radar surface current measurements: Intercomparisons with ship-based sensors. J. Geophys. Res., 102, 18737, https://doi.org/10.1029/97JC00049.
- CODAR, 2002: Defining first-order region boundaries. CODAR Ocean Sensors Ltd., Tech. Rep., 9 pp.
- Cook, T. M., T. DePaolo, and E. J. Terrill, 2007: Estimates of radial current error from high frequency radar using MUSIC for bearing determination. OCEANS 2007, IEEE, 6 pp., https:// doi.org/10.1109/OCEANS.2007.4449257.
- Cosoli, S., A. Mazzoldi, and M. Gačić, 2010: Validation of surface current measurements in the northern Adriatic Sea from highfrequency radars. *J. Atmos. Oceanic Technol.*, 27, 908–919, https://doi.org/10.1175/2009JTECHO680.1.
- —, G. Bolzon, and A. Mazzoldi, 2012: A real-time and offline quality control methodology for SeaSonde high-frequency radar currents. *J. Atmos. Oceanic Technol.*, 29, 1313–1328, https://doi.org/10.1175/JTECH-D-11-00217.1.
- de Paolo, T., and E. Terrill, 2007: Skill assessment of resolving ocean surface current structure using compact-antennastyle HF radar and the MUSIC direction-finding algorithm. *J. Atmos. Oceanic Technol.*, **24**, 1277–1300, https://doi.org/10.1175/JTECH2040.1.
- —, T. Cook, and E. Terrill, 2007: Properties of HF RADAR compact antenna arrays and their effect on the music algorithm. OCEANS 2007, IEEE, 10 pp., https://doi.org/10.1109/OCEANS.2007.4449265.
- Efron, B., and R. J. Tibshirani, 1994: An Introduction to the Bootstrap. CRC Press, 456 pp.
- Emery, B. M., 2018: HFR CS processing toolbox for MATLAB, v1.0. Zendo, https://doi.org/10.5281/zenodo.1451950.
- —, L. Washburn, and J. Harlan, 2004: Evaluating radial current measurements from CODAR high-frequency radars with moored current meters. *J. Atmos. Oceanic Technol.*, 21, 1259–1271, https://doi.org/10.1175/1520-0426(2004)021<1259: ERCMFC>2.0.CO;2.
- —, —, C. Whelan, D. Barrick, and J. Harlan, 2014: Measuring antenna patterns for ocean surface current HF radars with ships of opportunity. *J. Atmos. Oceanic Technol.*, **31**, 1564–1582, https://doi.org/10.1175/JTECH-D-13-00181.1.

- Forget, P., 2015: Noise properties of HF radar measurement of ocean surface currents. *Radio Sci.*, **50**, 764–777, https://doi.org/10.1002/2015RS005681.
- —, Y. Barbin, and G. André, 2008: Monitoring of surface ocean circulation in the Gulf of Lions (North-West Mediterranean Sea) using WERA HF radars. 2008 IEEE International Geoscience and Remote Sensing Symposium: Proceedings, Vol. I, IEEE, I375–I378, https://doi.org/10.1109/IGARSS.2008.4778872.
- Friedlander, B., 2009: Wireless direction-finding fundamentals. Classical and Modern Direction-of-Arrival Estimation, T. E. Tuncer and B. Friedlander, Eds., Elsevier, 1–51.
- Graber, H. C., B. K. Haus, R. D. Chapman, and L. K. Shay, 1997: HF radar comparisons with moored estimates of current speed and direction: Expected differences and implications. *J. Geophys. Res.*, 102, 18749–18766, https://doi.org/10.1029/97JC01190.
- Gurgel, K. W., G. Antonischki, H. H. Essen, and T. Schlick, 1999: Wellen Radar (WERA): A new ground-wave HF radar for ocean remote sensing. *Coastal Eng.*, 37, 219–234, https://doi.org/ 10.1016/S0378-3839(99)00027-7.
- Kirincich, A. R., 2017: Improved detection of the first-order region for direction-finding HF radars using image processing techniques. J. Atmos. Oceanic Technol., 34, 1679–1691, https:// doi.org/10.1175/JTECH-D-16-0162.1.
- —, T. De Paolo, and E. Terrill, 2012: Improving HF radar estimates of surface currents using signal quality metrics, with application to the MVCO high-resolution radar system. J. Atmos. Oceanic Technol., 29, 1377–1390, https://doi.org/10.1175/JTECH-D-11-00160.1.
- Kohut, J. T., and S. M. Glenn, 2003: Improving HF radar surface current measurements with measured antenna beam patterns. *J. Atmos. Oceanic Technol.*, 20, 1303–1316, https://doi.org/ 10.1175/1520-0426(2003)020<1303:IHRSCM>2.0.CO;2.
- ——, H. J. Roarty, and S. M. Glenn, 2006: Characterizing observed environmental variability with HF Doppler radar surface current mappers and acoustic Doppler current profilers: Environmental variability in the coastal ocean. *IEEE J. Oceanic Eng.*, 31, 876–884, https://doi.org/10.1109/JOE.2006.886095.
- Krim, H., and M. Viberg, 1996: Two decades of array signal processing research: The parametric approach. *IEEE Signal Process. Mag.*, 13, 67–94, https://doi.org/10.1109/79.526899.
- Lai, Y., H. Zhou, Y. Zeng, and B. Wen, 2017a: Accuracy assessment of surface current velocities observed by OSMAR-S high-frequency radar system. *IEEE J. Oceanic Eng.*, 43, 1068–1074, https://doi.org/10.1109/JOE.2017.2769179.
- —, —, and —, 2017b: Ocean surface current observation with a dual monopole-cross-loop antenna array. *Int. J. Antennas Propag.*, **2017**, 2754831, https://doi.org/10.1155/2017/2754831.
- —, —, and —, 2017c: Quantifying and reducing the DOA estimation error resulting from antenna pattern deviation for direction-finding HF radar. *Remote Sens.*, 9, 1285, https://doi.org/10.3390/rs9121285.
- Laws, K. E., D. M. Fernandez, and J. D. Paduan, 2000: Simulation-based evaluations of HF radar ocean current algorithms. *IEEE J. Oceanic Eng.*, 25, 481–491, https://doi.org/10.1109/48.895355.
- —, J. D. Paduan, and J. Vesecky, 2010: Estimation and assessment of errors related to antenna pattern distortion in CODAR SeaSonde high-frequency radar ocean current measurements. J. Atmos. Oceanic Technol., 27, 1029–1043, https://doi.org/ 10.1175/2009JTECHO658.1.
- LeVeque, R. J., 2007: Finite Difference Methods for Ordinary and Partial Differential Equations: Steady-State and Time-Dependent Problems. Classics in Applied Mathematics, SIAM, 184 pp.

- Lipa, B. J., and D. E. Barrick, 1983: Least-squares methods for the extraction of surface currents from CODAR crossed-loop data: Application at ARSLOE. *IEEE J. Oceanic Eng.*, 8, 226– 253, https://doi.org/10.1109/JOE.1983.1145578.
- —, B. Nyden, D. S. Ullman, and E. Terrill, 2006: SeaSonde radial velocities: Derivation and internal consistency. *IEEE J. Oceanic Eng.*, 31, 850–861, https://doi.org/10.1109/ JOE.2006.886104.
- Liu, Y., R. H. Weisberg, C. R. Merz, S. Lichtenwalner, and G. J. Kirkpatrick, 2010: HF radar performance in a low-energy environment: CODAR SeaSonde experience on the West Florida Shelf. J. Atmos. Oceanic Technol., 27, 1689–1710, https://doi.org/10.1175/2010JTECHO720.1.
- —, and —, 2014: Assessment of CODAR SeaSonde and WERA HF radars in mapping surface currents on the West Florida shelf. *J. Atmos. Oceanic Technol.*, **31**, 1363–1382, https://doi.org/10.1175/JTECH-D-13-00107.1.
- Lorente, P., J. Soto-Navarro, E. Alvarez Fanjul, and S. Piedracoba, 2014: Accuracy assessment of high frequency radar current measurements in the Strait of Gibraltar. J. Oper. Oceanogr., 7 (2), 59–73, https://doi.org/10.1080/1755876X.2014.11020300.
- Molcard, A., P. M. Poulain, P. Forget, A. Griffa, Y. Barbin, J. Gaggelli, J. C. De Maistre, and M. Rixen, 2009: Comparison between VHF radar observations and data from drifter clusters in the Gulf of La Spezia (Mediterranean Sea). J. Mar. Syst., 78, S79–S89, https://doi.org/10.1016/j.jmarsys.2009.01.012.
- O'Donnell, J., and Coauthors, 2005: Integration of Coastal Ocean Dynamics Application Radar (CODAR) and Short-Term Predictive System (STPS) surface current estimates into the Search and Rescue Optimal Planning System (SAROPS). U.S. Coast Guard Research and Development Center Rep. CG-D-01-2006, 163 pp.
- Ohlmann, C., P. White, L. Washburn, E. Terrill, B. Emery, and M. Otero, 2007: Interpretation of coastal HF radar-derived surface currents with high-resolution drifter data. *J. Atmos. Oceanic Technol.*, 24, https://doi.org/10.1175/JTECH1998.1.
- Oke, P. R., J. S. Allen, R. N. Miller, G. D. Egbert, and P. M. Kosro, 2002: Assimilation of surface velocity data into a primitive equation coastal ocean model. *J. Geophys. Res.*, 107, 3122, https://doi.org/10.1029/2000JC000511.
- Orfila, A., A. Molcard, J. M. Sayol, J. Marmain, L. Bellomo, C. Quentin, and Y. Barbin, 2015: Empirical forecasting of HF-radar velocity using genetic algorithms. *IEEE Trans. Geosci. Remote Sens.*, 53, 2875–2886, https://doi.org/10.1109/TGRS.2014.2366294.
- Paduan, J. D., K. C. Kim, M. S. Cook, and F. P. Chavez, 2006: Calibration and validation of direction-finding high-frequency radar ocean surface current observations. *IEEE J. Oceanic Eng.*, 31, 862–875, https://doi.org/10.1109/JOE.2006.886195.
- Pierson, W. J., and L. Moskowitz, 1964: A proposed spectral form for fully developed wind seas based on the similarity theory of S. A. Kitaigorodskii. J. Geophys. Res., 69, 5181–5190, https:// doi.org/10.1029/JZ069i024p05181.
- Romero, L., D. A. Siegel, J. C. McWilliams, Y. Uchiyama, and C. Jones, 2016: Characterizing storm water dispersion and dilution from small coastal streams. *J. Geophys. Res. Oceans*, 121, 3926–3943, https://doi.org/10.1002/2015JC011323.
- Schmidt, R., 1986: Multiple emitter location and signal parameter estimation. *IEEE Trans. Antennas Propag.*, 34, 276–280, https://doi.org/10.1109/TAP.1986.1143830.
- Sentchev, A., P. Forget, Y. Barbin, and M. Yaremchuk, 2013: Surface circulation in the Iroise Sea (W. Brittany) from high resolution HF radar mapping. J. Mar. Syst., 109–110 (Suppl.), S153–S168, https://doi.org/10.1016/j.jmarsys.2011.11.024.

- Shchepetkin, A. F., and J. C. McWilliams, 2005: The regional oceanic modeling system (ROMS): A split-explicit, freesurface, topography-following-coordinate oceanic model. *Ocean Modell.*, 9, 347–404, https://doi.org/10.1016/j.ocemod.2004.08.002.
- Skamarock, W. C., J. B. Klemp, J. Dudhia, D. O. Gill, D. M. Barker, W. Wang, and J. G. Powers, 2005: A description of the Advanced Research WRF version 2. NCAR Tech. Note NCAR/TN-468+STR, 88 pp., https://doi.org/10.5065/D6DZ069T.
- Stoica, P., and R. L. Moses, 2005: *Spectral Analysis of Signals*. Pearson Prentice Hall, 452 pp.
- —, and A. Nehorai, 1989: Music, maximum likelihood, and Cramer-Rao bound. *IEEE Trans. Acoust. Speech Signal Process.*, **37**, 720–741, https://doi.org/10.1109/29.17564.
- Tian, Y., B. Wen, J. Tan, and Z. Li, 2017: Study on pattern distortion and DOA estimation performance of crossed-loop/monopole

- antenna in HF radar. *IEEE Trans. Antennas Propag.*, **65**, 6095–6106, https://doi.org/10.1109/TAP.2017.2755442.
- Tuncer, E., and B. Friedlander, 2009: Classical and Modern Directionof-Arrival Estimation. T. E. Tuncer and B. Friedlander, Academic Press, 456 pp.
- Uchiyama, Y., E. Y. Idica, J. C. McWilliams, and K. D. Stolzenbach, 2014: Wastewater effluent dispersal in Southern California Bays. *Cont. Shelf Res.*, **76**, 36–52, https://doi.org/10.1016/j.csr.2014.01.002.
- Van Trees, H. L., 2002: Optimum Array Processing: Part IV of Detection, Estimation and Modulation Theory. John Wiley & Sons, 1472 pp., https://doi.org/10.1002/0471221104.
- Xu, X.-L., and K. M. Buckley, 1992: Statistical performance analysis of the MUSIC location estimator. *IEEE Trans. Signal Process.*, 40, 2559–2569, https://doi.org/10.1109/78.157296.